



## Solar selective absorbing coatings based on AlSiN/AlSiON/AlSiO<sub>y</sub> layers



L. Rebouta<sup>a,\*</sup>, A. Sousa<sup>a</sup>, M. Andritschky<sup>a</sup>, F. Cerqueira<sup>a</sup>, C.J. Tavares<sup>a</sup>, P. Santilli<sup>b</sup>, K. Pischow<sup>b</sup>

<sup>a</sup> Centre of Physics, University of Minho, Alameda da Universidade, 4804-533 Guimarães, Portugal

<sup>b</sup> Savo Solar Oy, Insinöörinkatu 7, 50100 Mikkeli, Finland

### ARTICLE INFO

#### Article history:

Received 18 March 2015

Received in revised form 21 July 2015

Accepted 28 July 2015

Available online 1 August 2015

#### Keywords:

Solar selective absorber

AlSiN/AlSiON/AlSiO<sub>y</sub>

Optical constants

Dielectric function modelling

Thermal stability

### ABSTRACT

Coatings with a double absorbing layer based on AlSiN/AlSiON were deposited on stainless steel substrates by magnetron sputtering technique, with different Al:Si ratios. A tungsten layer was used as a back reflector and AlSiO<sub>y</sub> or SiO<sub>x</sub> thin films were used as antireflection top layers. Prior the structure design, several single layers were deposited on glass substrates by varying the reactive gases flows, which allowed the stacking of a series of layers with different optical properties. Experimental transmittance and reflectance were modelled for the assessment of the spectral optical constants, which were then used to design a coating stack with optimized solar absorptance and thermal emittance. Optical properties, microstructure, morphology, composition and chemical bonding were investigated by employing optical spectroscopy, scanning electron microscopy, energy dispersive X-ray spectroscopy, X-ray diffraction and X-ray photoelectron spectroscopy. The samples were annealed in air at 400 °C and vacuum at 580 °C with the purpose to evaluate their oxidation resistance and thermal stability, which was subsequently correlated with the Al:Si ratio. Optimum results were achieved for an Al:Si ratio of 2.3:1, whereas for significantly higher Si content resulted in detrimental performance. The solar absorbanse and thermal emittance for the optimized multilayer selective coatings is 93–94% and 7–10% (at 400 °C), respectively.

© 2015 Elsevier B.V. All rights reserved.

## 1. Introduction

Development of solar selective absorbing coatings for photothermal conversion started originally in the 70s [1–4], where studies for applications for electricity generation were already included [5]. It is being prospected for the near future a growth in the number of concentrated solar power (CSP) plants all over the world for electricity generation. This development should be accompanied with an efficiency increase of the involved systems, aligned with a decrease of its costs. The main requirements for solar selective absorbing coatings are high absorptance ( $\alpha$ ) in the wavelength range of 0.3–2.0  $\mu\text{m}$  and low thermal emittance ( $\varepsilon$ ) in the infrared (IR) region ( $>2.0 \mu\text{m}$ ). The global efficiency can be increased by a decrease of the thermal emittance and an increase of solar absorptance, whereas the global costs can be reduced by the increase of the long term stability.

The coatings are based in a bilayer structure, where the solar absorptance is optimized through the interference effect. According to the double interference absorption theory [6–8], the coating must have a layered structure consisting of an IR-reflective metallic base layer, a double interference absorption layer and a ceramic anti-reflection (AR) top layer. The design can be done with ceramic–metal composite (cermet) coatings, where the metal volume fraction is used to adjust the refractive index of each layer [9–13], or with other kind of materials with adequate refractive index and extinction coefficient [14–16].

AlSiON is known due to several interesting mechanical, chemical and thermal properties [17,18], which makes them good candidates for high temperature applications. In this work it is presented the results of a solar selective absorbing coating based on W/AlSiN/AlSiON/AlSiO<sub>y</sub> layers, which is a potential candidate for intermediate temperature absorbers to be used in a solar concentration system. Within the frame of this work, solar selective absorbing coating stacks were developed based on AlSiN and AlSiON ceramic layers with different Al:Si ratios.

\* Corresponding author.

E-mail address: [rebouta@fisica.uminho.pt](mailto:rebouta@fisica.uminho.pt) (L. Rebouta).

**Table 1**

Targets and deposition mode for coatings with different Al:Si ratio.

Coating type	Target	Deposition mode
SAON1	Al + 9 Si discs	Static
SAON2	Al + 15 Si discs	Static
SAON3	SiAl (70/30)	Static
SAON4	Al + 9 Si discs	Rotation

## 2. Experimental details

### 2.1. Sample preparation and characterization

The W metallic back layer was deposited by DC magnetron sputtering in static mode from a pure tungsten target, using a current density of 8 mA/cm<sup>2</sup>. The deposition rate was ~60 nm/min. Four types of absorber coatings were optimized and tested using three different targets (different Al:Si ratio) and different deposition modes, as described in Table 1. The AlSiN and AlSiON layers were deposited also by DC sputtering using an Al target (10 cm diameter), with small silicon discs (diameter of 1 cm) within the erosion zone (9 discs in the first series and 15 in the second series of samples), and from a SiAl target (70/30). For the first Al:Si ratio (9 Si discs), coatings in both static mode and rotation mode were prepared. Static mode represents the deposition where substrates were stopped for a predetermined time on top of each target, whereas rotation mode refers to substrates rotating with a determined angular speed (15 rpm) over the targets. Single layers (AlSiN, AlSiON and AlSiO<sub>y</sub>) were prepared using a target current density of 5 mA/cm<sup>2</sup>. Argon was used as working gas. AlSiN layers were produced employing solely nitrogen as a reactive gas and for AlSiON layers a reactive gas mixture (nitrogen + oxygen with an 85:15 ratio) was used. The AR layers, based on AlSiO<sub>y</sub> thin films, were prepared under an Ar/O<sub>2</sub> atmosphere. Prior to the deposition, the vacuum chamber was evacuated to a base pressure of  $2 \times 10^{-4}$  Pa and during all depositions a pulsed bias of -60 V (frequency 90 kHz) was applied to the substrate holder. These multilayer stacks were deposited on polished stainless steel substrates (25 mm × 25 mm × 1 mm).

The SiO<sub>2</sub> layer was deposited by plasma enhanced chemical vapour deposition (PECVD) assisted with an inductively coupled plasma (ICP) source using octamethylcyclotetrasiloxane (OMCTS), [(CH<sub>3</sub>)<sub>2</sub>SiO]<sub>4</sub> as a precursor [19].

The crystalline structure of the absorber coating was studied using X-ray diffraction employing a Bruker AXS Discover D8 operating with Cu K $\alpha$  radiation. X-ray diffraction measurements were performed at an incidence angle of 3°. Scanning electron microscopy (SEM) was performed with a NanoSEM-FEI Nova 200 (FEG/SEM) microscope. Energy dispersive X-ray spectroscopy (EDS) analyzes were performed with the electron beam of the SEM, with an energy of 13.5 keV (EDAX – Pegasus X4M system). Optical measurements, in transmittance and reflectance modes, were performed in the wavelength range of 0.25–2.5 μm, using a Shimadzu PC3100 spectrophotometer. The reflectance measurements were performed at an incidence angle of 8° using an integrating sphere attachment and an Al mirror as a reference. The reflectance data were corrected accordingly with the Al-reference reflectance curve. The normal solar absorptance,  $\alpha_{\text{sol}}$ , is defined as a weighted fraction between absorbed radiation and incoming solar radiation and was determined using either calculated or experimentally obtained spectral reflectance data  $R(\lambda)$  and ASTM AM1.5D solar spectral irradiance,  $I_s(\lambda)$ , according to [3]:

$$\alpha_{\text{sol}} = \frac{\int_{0.3 \mu\text{m}}^{2.5 \mu\text{m}} I_s(\lambda)[1 - R(\lambda)]d\lambda}{\int_{0.3 \mu\text{m}}^{2.5 \mu\text{m}} I_s(\lambda)d\lambda} \quad (1)$$

A Fourier transform infrared (FTIR) spectrophotometer from Agilent Technologies equipped with a gold integrating sphere and a MCT detector was used to measure the spectral reflectance in the infrared wavelength range, 1.6–16.7 μm. The normal thermal emittance,  $\varepsilon_{\text{th}}$ , is a weighted fraction between emitted radiation and the Planck black body distribution at a specific temperature and was calculated from [3]:

$$\varepsilon_{\text{th}} = \frac{\int_{1.6 \mu\text{m}}^{25 \mu\text{m}} I_{bb}(\lambda)[1 - R(\lambda)]d\lambda}{\int_{1.6 \mu\text{m}}^{25 \mu\text{m}} I_{bb}(\lambda)d\lambda} \quad (2)$$

where  $I_{bb}(\lambda)$  is the spectral blackbody emissive power and  $R(\lambda)$  the spectral reflectance. A gold thin film was used as a reference for these reflectance measurements. Considering that gold has an absolute reflectance lower than 100%, a polished copper plate was used to correct it. The reflectance of the copper plate was measured and corrected multiplying their reflectance by a constant factor (smaller than 1) in order to obtain a thermal emittance of 3%. This correction was applied to all IR reflectance measurements. The emittance was also measured (at 80 °C) with an emissometer AE-AD3, from Devices & Service Company.

The chemical analysis was performed using a Kratos AXIS Ultra HSA X-ray photoelectron spectroscopy (XPS) system, with an Al K $\alpha$  (1486.7 eV) X-ray source. The spectra were modelled using the XPSPEAK41 software and the peaks were assumed to have a Gaussian-Lorentzian shape, and a Shirley type background was considered.

Raman scattering measurements were carried out at room temperature in a back scattering geometry on alpha300 R confocal Raman microscope (WITec) using a 532 nm Nd:YAG laser for excitation. The system was operated with an output laser power of ≈1.5 mW and the Raman signal was acquired using 2 s and 30 acquisitions for each spectra.

The accelerated ageing studies in air were performed in a Termolab air furnace at a temperature of 400 °C. The furnace has a K-type thermocouple for temperature measurements and the temperature was controlled with a Shimaden FP21 programmable controller. The vacuum thermal treatments (pressure  $< 6 \times 10^{-4}$  Pa) were also performed in a Termolab furnace with same type of controller and at a temperature of 580 °C. A K-type thermocouple for temperature measurements was fixed inside the sample holder.

### 2.2. Calculation of optical constants of single layers and optical design of the coating

The spectral optical constants of single layers can be determined from transmittance ( $T$ ) and reflectance ( $R$ ) [20,21].  $R$  and  $T$  curves were modelled by a commercial optical simulation programme (SCOUT) [22] and the thickness and dielectric function of the different layers were calculated. The model used in the calculations assumes that there are several different types of oscillators, each with their own characteristic resonant frequency. This enables the calculation of the frequency dependence of the complex dielectric constant,  $\tilde{\epsilon}_r = \epsilon_1 + i\epsilon_2$ , which can be used to obtain the optical constants,  $n$  and  $k$ , being  $n$  the normal refractive index and  $k$  the extinction coefficient. This is performed through the relation between the complex dielectric constant and the complex refractive index,  $\tilde{n}^2 = \tilde{\epsilon}_r$ , where the complex refractive index is usually defined as  $\tilde{n} = n + ik$  [20,21]. With this process, and for each single layer, the optical constants ( $n$  and  $k$ ) as a function of the wavelength and coating thickness (and deposition rate) were obtained. Thus, the first step was the preparation of different single layers of: AlSiN and AlSiON with varying content of nitrogen and oxygen; the back reflector, W; and the antireflection layers, AlSiO<sub>y</sub> and SiO<sub>2</sub>.  $R$

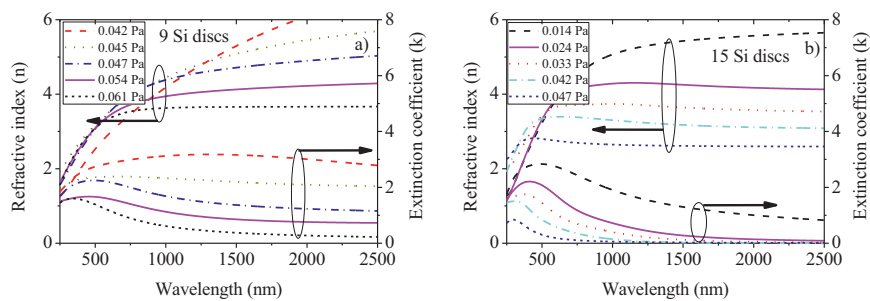


**Fig. 1.** Refractive index ( $n$ ) and extinction coefficient ( $\kappa$ ) of nitrides, prepared with increasing nitrogen partial pressure, as indicated in the legend, and obtained with (a) Al target with 9 Si discs (series 1) and (b) Al target with 15 Si discs (series 2).

**Table 2**

Deposition parameters for individual layers used to build the multilayer stacks. The target current density and substrate bias voltage remained constant.

Nitride layer (HA)	N <sub>2</sub> partial pressure (Pa)	Deposition time (s)	Deposition rate [nm/min]	Al/Si ratio	Oxynitride layer (LA)	N <sub>2</sub> /O <sub>2</sub> (85:15) partial pressure (Pa)	Deposition time (s)	Deposition rate [nm/min]	Al/Si ratio
<b>Al/(9Si) – Static mode</b>									
9.N1	0.042	90	60		9.NO1	0.061	90	48	2.2
9.N2	0.047	90	60	2.1	9.NO2	0.077	90	36	2.4
9.N3	0.054	90	54	2.5	9.NO3	0.095	90	36	
<b>Al/(15Si) – Static mode</b>									
15.N1	0.014	60	78		15.NO1	0.045	90	53	
15.N2	0.024	60	78	1.4	15.NO2	0.049	90	50	0.8
15.N3	0.033	90	60	1.3	15.NO3	0.061	90	36	0.7
15.N4	0.047	90	48		15.NO4	0.077	90	30	
<b>Si70/Al30 – Static mode</b>									
SA.N1	0.010	60	78	0.4	SA.NO3	0.049	90	52	0.4
SA.N2	0.014	60	75		SA.NO4	0.061	90	48	
SA.N3	0.024	60	74	0.5	SA.NO5	0.077	90	42	0.4
<b>Al/(9Si) – Rotation mode</b>									
9.N1r	0.047	300	14		9.NO1r	0.061	300	11	2.8

and  $T$  curves were measured and modelled with SCOUT [22], for the assessment of the spectral optical constants, as mentioned above.

After the determination of the spectral optical constants of the aforementioned different layers it is then possible to build a multilayer structure with the desired optical spectra ( $T$  and  $R$ ), as well as its optimization. The SCOUT software was used to design four layers coating stacks with optimized absorptance  $\alpha_s$  and emissivity  $\varepsilon_s$ . This modelling step allows for selecting the materials to be used with respective thicknesses. Finally, the multilayered coating was deposited onto a polished stainless steel substrate, using the layered materials and thicknesses selected in the modelling step.

### 3. Results

#### 3.1. Optical properties of single layers

Three series multilayer stacks were studied based on the target composition: (1) 9 Si discs on Al target; (2) 15 Al disc on Al target; (3) a Si70Al30 target. All these structures were prepared in static mode. A fourth series was prepared in rotation mode, using the first target composition (9 Si discs on Al target) as described in Table 1. Concerning the high absorbing layer, for each series a set of individual layers was deposited varying the nitrogen partial pressure, in order to vary the optical properties from low to medium transparency. In the first series (Fig. 1a) the nitrogen partial pressure was varied from 0.042 Pa to 0.061 Pa. In the second series (Fig. 1b) the nitrogen partial pressure was varied from 0.014 to 0.047 Pa, while in the third series (not shown) it varied from 0.010 to 0.033 Pa. The deposition rates of representative layers are indicated in Table 2, within the mentioned nitrogen partial pressure ranges. The low absorbing layer was deposited using nitrogen and oxygen as reactive gases, and both were varied with constant ratio (85:15 as it

is indicated in Table 2). The thicknesses of these individual layers are between 50 and 90 nm. The spectral optical constants ( $n$  and  $\kappa$ ) were calculated and are presented in Fig. 1 (nitrides, HA layers) and Fig. 2 (oxynitrides, LA layers), for the first two series (series 1 Al target with 9 Si discs and series 2–15 Si discs, respectively). With increasing nitrogen partial pressure, the AlSiN layers become more transparent and lose their metallic behaviour, as expected due to the inherent optical properties of AlN and Si<sub>3</sub>N<sub>4</sub>.

From the obtained optical constants (Figs. 1 and 2) it can be seen that the Al:Si ratio has also an important role in the tailoring of the optical properties. The high absorbing layer should have an increasing refractive index in the wavelength range 0.4–1.0  $\mu$ m, varying approximately from 2.5 to 5. This allows, for the same thickness, an optical path ( $n \cdot d$  = refractive index  $\times$  thickness) of about  $\lambda/4$  for different wavelengths in order to improve the interference effect. This strategy was accomplished for the first series (9 Si discs) samples produced with a nitrogen partial pressure of 0.047 and 0.054 Pa (Fig. 1a), which have an extinction coefficient  $\sim 1$  (also important for intrinsic absorption). With the increase of the Si content in the films (Fig. 1b), the refractive index variation becomes limited to a smaller wavelength range and the layers also become more transparent, with a lower extinction coefficient. For higher Si content (lower Al:Si ratio) it was necessary to produce the nitride films with lower N<sub>2</sub> partial pressure and oxynitride films with lower N<sub>2</sub>/O<sub>2</sub> partial pressures (Table 2), when compared with similar films obtained for higher Al:Si ratio. This means that were used nitrides with some nitrogen deficiency, which may affect the chemical stability.

The spectral optical constants for the antireflection layers are shown in Fig. 3, where it is presented the optical constants of the SiO<sub>2</sub> layer prepared by PECVD and AlSiO<sub>y</sub> layers prepared by sputtering with Al targets having 9 and 15 Si discs. The extinction coefficient is small in all cases ( $\sim 0$ ). The SiO<sub>2</sub> layer has a

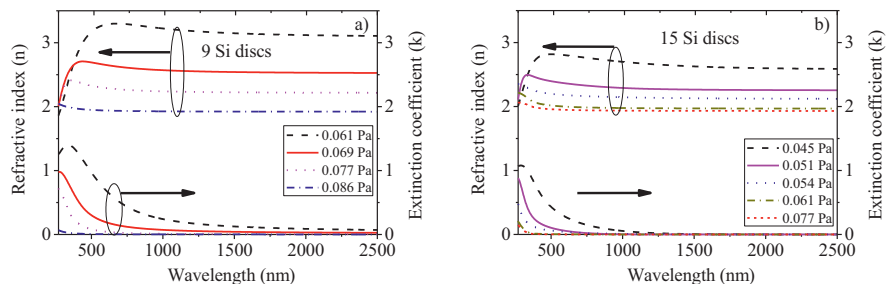


**Fig. 2.** Refractive index ( $n$ ) and extinction coefficient ( $\kappa$ ) of oxynitrides, prepared with increasing nitrogen and oxygen partial pressures, as indicated in the legend, and obtained with (a) Al target with 9 Si discs (series 1) and (b) Al target with 15 Si discs (series 2).

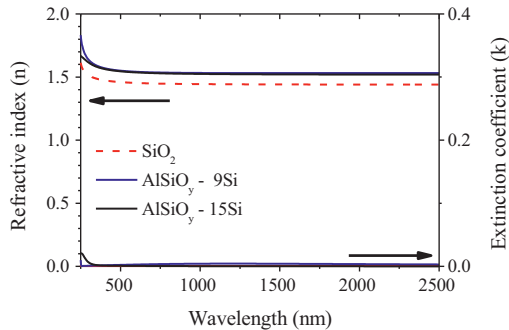


**Fig. 3.** Refractive index ( $n$ ) and extinction coefficient ( $\kappa$ ) of antireflection layers used in multilayers,  $\text{SiO}_2$  prepared by PECVD, and  $\text{AlSiO}_y$  prepared with Al target with 9 Si discs and 15 Si discs.

refractive index of about 1.48, while the others have a slightly higher index (~1.53) due to the Al content. Although the refractive index is slightly higher than that of  $\text{SiO}_2$ , the use of these AR layers has the advantage of using the same target for HA, LA and AR layers.

The composition of some of these layers was measured by EDS. For layers prepared with the Al target having 9 Si discs, the nitrides and oxynitrides revealed a similar Al/Si atomic ratio of ~2.3. However, in the oxide layer this ratio decreased to about 0.5. As it will be shown in next section, the nitrides are sub-stoichiometric, which means that the poisoning effect on the target surface during deposition is negligible. However, during oxide deposition, an oxide layer is formed on the target surface, which usually yields a decrease of the sputtering rate. The  $\text{Al}_2\text{O}_3$  sputtering rate is an order of magnitude lower than that of Al [23]. On the other hand, the sputtering rates in nm/s of Si and  $\text{SiO}_2$  are similar [24], which means that the oxide formation at Al and Si surfaces induces a higher reduction on the Al sputtering rate than that of Si, leading to the aforementioned decrease in the Al/Si atom ratio. For the case of layers prepared with 15 Si discs, the absorbing layer revealed an Al/Si atomic ratio of ~1.35, while the oxynitrides showed a ratio of 0.75.

### 3.2. Chemical state and composition of the $\text{AlSiN}/\text{AlSiON}$ films

In order to assess the detailed chemical information of the films, three individual layers were prepared with the same parameters as of those used in a multilayer stack and subsequently analyzed by XPS. Such layers correspond to the nitride 9.N2 (A), the oxynitride 9.NO1 (B), both were optically characterized in Figs. 1a and 2a and Table 2, and an oxide (C). Spectra of Al 2p, Si 2p, N 1s and O 1s were evaluated and the characteristic peaks of Si, Al, N and O were all observed and are represented in Fig. 4. The carbon peak (not shown), was assumed to correspond to a binding energy located at 285.0 eV and was used as a reference for all binding energies. Table 3 presents the results of the spectra decomposition for the

four samples. In the case of nitride (A), the Al (2p) core level binding energy, depicted in Fig. 4a, is deconvoluted in two distinct components (73.0 eV and 74.5 eV), of a simple Gaussian shape, both with a full width at half maximum (FWHM) of 1.4 eV. It was considered that the FWHM of these peaks should be similar for the other samples. Thus, for the deconvolution of Al (2p) core level binding energy of sample B it was necessary to include one more peak (centred at 73.7 eV). In sample C, a fourth peak, centred at 75.5 eV, was considered, which is consistent with the presence of Al oxide [25,26]. The atomic ratio N/(Al + Si) of sample A is about 1/3. Then, in  $\text{AlSiN}$  films, the number of incorporated N atoms is insufficient to form the respective nitride, which enables the creation of intrinsic defects such as Al–Si, Al–Al or Si–Si bonds. The peak at 73.0 eV can be assigned to Al–Si or Al–Al bonds, in excellent agreement with the literature data obtained for pure Al and Al–Si alloys [25–27]. Both peaks located at the binding energies of 74.5 and 75.5 eV are present in sample C (oxide), which has no nitrogen, and corresponds to the formation of  $\text{Al}(\text{OH})_3$  and  $\text{Al}_2\text{O}_3$  compounds, respectively. However, the peak at 74.5 eV can also be due the presence of O–Al–N bonds [28], which can occur in sample A (nitride). Finally the peak at 73.7 eV can be assigned to the Al–N bonds [28,29]. The binding energy separation between the peak associated with Al–Si and Al–Al bonds (73.0 eV) and the oxide peak (75.5 eV) is 2.5 eV, which is similar to the value of 2.7 eV found between metallic Al and Al oxide components [25,26].

Regarding the Si 2p spectra, shown in Fig. 4b, the spectra for samples A and B were decomposed in four distinct components (98.1 eV, 99.2, 100.8 eV and 101.9 eV). Of the former peaks, in sample C it was maintained only the peak at 101.9 eV and it was necessary to include a fifth peak centred at 103.1 eV. For the analysis of XPS silicon peaks, it has been reported in the literature a model that describes the composition and structure of the oxynitride film, which is the random bonding model [30,31]. According to this model, the five peaks obtained from the spectra fitting would correspond to a decreasing partial charge on the Si atom. Accordingly to the mentioned model, the peak located at 98.1 eV corresponds to Si–Si or Si–Al bonds, considering the N deficiency in sample A, while the peak located at 103.1 eV can be assigned to Si oxide ( $\text{Si}(\text{Al})-\text{SiO}_3$  and  $\text{Si}-\text{O}_4$  bonds) and possibly to  $\text{Si}-\text{O}_3\text{N}$  and  $\text{Si}-\text{O}_2\text{N}_2$  bonds [31,32]. The binding energy separation between the peak associated with Al–Si and Si–Si bonds (98.1 eV) and the oxide peak (103.1 eV) is 5.0 eV, which is higher than the reported value of ~4.0 eV between the Si–Si peak in pure silicon and the Si oxide peak [31,33,34].

The peak located at 99.2 eV can be ascribed to a  $\text{Si}(\text{Al})-\text{Si}_3\text{N}$  and  $\text{Si}(\text{Al})-\text{Si}_3\text{O}$  bonds and the peak located at 100.8 eV can be ascribed to a  $\text{Si}(\text{Al})-\text{Si}_2\text{N}_2$  and  $\text{Si}(\text{Al})-\text{Si}_2\text{ON}$  bonds. Finally, the 101.9 eV peak corresponds to the formation of silicon oxynitrides due to the level of oxygen content ( $\text{SiN}_3\text{O}$ ;  $\text{Si}(\text{Al})-\text{SiO}_2\text{N}$  and  $\text{Si}(\text{Al})-\text{SiON}_2$  bonds) and silicon nitride ( $\text{Si}-\text{N}_4$  bond) [29–31]. The binding energies obtained for the Si peak and its identification are presented in Table 3.

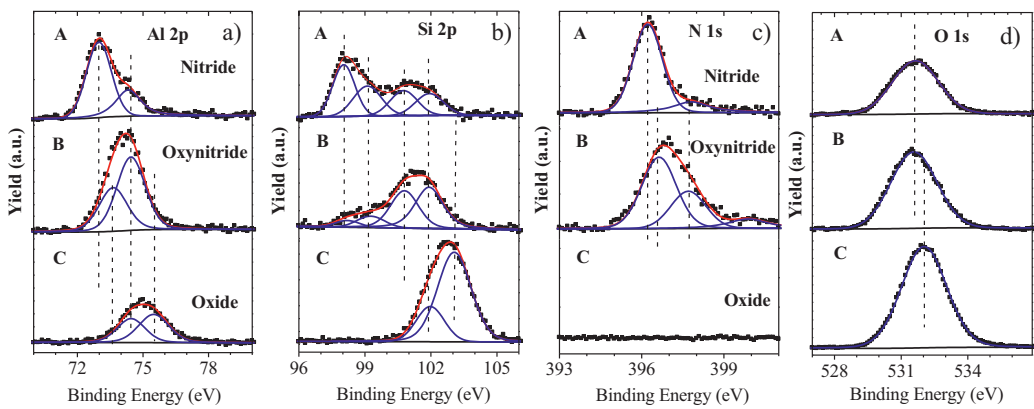


**Fig. 4.** XPS spectra of: (a) Al 2p, (b) Si 2p, (c) N 1s and (d) O 1s electrons for analyzed samples.

**Table 3**  
Identification of core level binding energies for Al 2p, Si 2p and N 1s of analyzed samples.

Sample Core level	A BE (eV)	B BE (eV)	C BE (eV)	
Al 2p	73.0	–	–	Al-Al; Al-Si
	73.7	73.7	–	Al-N
	74.4	74.4	74.5	Al-OH
	–	75.5	75.5	Al-O
	98.1	98.2	–	Si-Si; Si-Al
Si 2p	99.2	99.3	–	Si(Al)-Si <sub>3</sub> N; Si(Al)-Si <sub>3</sub> O
	100.8	100.8	–	Si(Al)-Si <sub>2</sub> N <sub>2</sub> ; Si(Al)-Si <sub>2</sub> ON
	101.9	101.9	102.0	Si-N <sub>4</sub> ; Si(Al)-Si <sub>2</sub> O <sub>2</sub> ; Si(Al)-Si <sub>2</sub> O <sub>2</sub> N; Si(Al)-SiON <sub>2</sub> ; Si(Al)-SiO <sub>3</sub> ; Si-O <sub>4</sub>
	–	–	103.1	Si(Al)-SiO <sub>3</sub> ; Si-O <sub>4</sub>
	396.2	396.6	–	Al-N
N 1s	397.8	397.7	–	Si-N <sub>4</sub> ; Si(Al)-SiON <sub>2</sub> ; Si(Al)-Si <sub>2</sub> (Al)ON
	–	399.9	–	Si(Al)-O <sub>2</sub> N <sub>2</sub> ; Si(Al)-O <sub>3</sub> N

**Fig. 4c** shows the binding energy results of N 1s. Sample A has a main peak located at 396.2 eV, with a FWHM of 1.4 eV, and a small peak located at 397.8 eV. The first peak can be ascribed to N-Al bonds [28,35]. The second can be related with N-Si [28,29,31], but can also be assigned to Al and Si oxynitrides [27,31,33,34], which would correspond to having oxygen atoms as second-nearest-neighbour atoms. In sample B the first peak shifts to 396.4 eV, which can be justified by the increase of N-Al-O and N-Si-O bonds. The peak with highest energy appears in sample B at 399.9 eV and is ascribed to Al and Si oxynitride, where oxygen atoms are already first-nearest-neighbour atoms [18,28,34,36], which happens when the oxygen concentration gets large enough [37].

Regarding the O 1s spectra, shown in **Fig. 4d**, in the nitride (sample A), the O 1s peak is located at a binding energy of 531.6 eV, which shifts to 532.0 eV in the oxide (sample C). These peaks have a FWHM of about 2.5 eV and should have at least four components. However these peaks were not deconvoluted in its components because their respective energies are not evidently discerned. Nevertheless, these peaks can be assigned to Si-O and Al-O bonds (532 eV [26], and to the oxygen in the hydroxyl groups (-OH) (Al hydroxide 533.4 eV in [26]).

XPS can also provide information about the composition and relative atomic concentrations of elements were obtained from survey scans with the spectrometer working with a 40 eV pass energy and by dividing the integrated intensity values by their sensitivity

**Table 4**  
Atomic composition of different samples obtained from XPS analyzes (carbon is not included).

	Al 2p	Si 2p	N 1s	O 1s	Al/Si	Al/Si (EDS)
A (at%)	30.9	17.3	16.8	35.0	1.8	2.1 ± 0.4
B (at%)	31.0	12.4	17.4	39.3	2.5	2.2 ± 0.4
C (at%)	14.8	22.5	0	62.7	0.7	0.5 ± 0.1

factors. From corresponding Al 2p, Si 2p, N 1s and O 1s core-level intensities and tabulated atomic sensitivity factors (0.78 for O 1s, 0.477 for N 1s, 0.193 for Al 2p and 0.328 for Si 2p), the relative atomic concentrations were calculated and are presented in **Table 4**.

The oxygen and nitrogen content are sensitive to the superficial contamination, but the atomic Al to Si ratio is less sensitive to that. The same samples were characterized by EDS and a similar Al:Si ratio was obtained. The presence of Al-Al and Al-Si bonds associated with amounts of oxygen and nitrogen confirm that the films are substoichiometric.

### 3.3. X-ray diffraction of single layers

Thick layers of W, AlSiN and AlSiON layers were deposited and subsequently analyzed by X-ray diffraction. In **Fig. 5** are represented the XRD patterns of a W single layer (**Fig. 5a**) and AlSiN, AlSiON and AlSiO<sub>y</sub> layers prepared with the higher Al to Si ratio (**Fig. 5b**). The W layer is polycrystalline with [1 1 0] orientation. The patterns of AlSi nitride, oxynitride and oxide layers reveal a shoulder, which is characteristic of the amorphous glass substrate. The absence of diffraction peaks shows that these layers are amorphous.

### 3.4. Development of the W/AlSiN/AlSiON/SiO<sub>2</sub> optical stacks

The deposition parameters of the W layer were maintained constant for all multilayers and with a thickness of about 150 nm. When the Al/9Si target was used, the multilayers (both in static and in rotation mode) were built with 4 layers, as schematically represented in **Fig. 6a**. With the Al/15Si and Si70Al30 targets, the absorbing layers were not sufficiently absorptive and it was necessary to increment the interference effect, and two additional layers (six in total) were used, as represented in **Fig. 6b**.

As previously mentioned, the structure of the multilayers was optimized by the simulation of its reflectance, varying the materials characterized in Section 3.1 and its thicknesses. From this optimization procedure, the deposition parameters were selected for different layers, such as reactive gas partial pressure and respective thickness. In **Table 5** are presented the single layers used in each coating, which are identified by the reactive gas partial pressure, as were identified in **Figs. 1–3** and respective thicknesses. All the

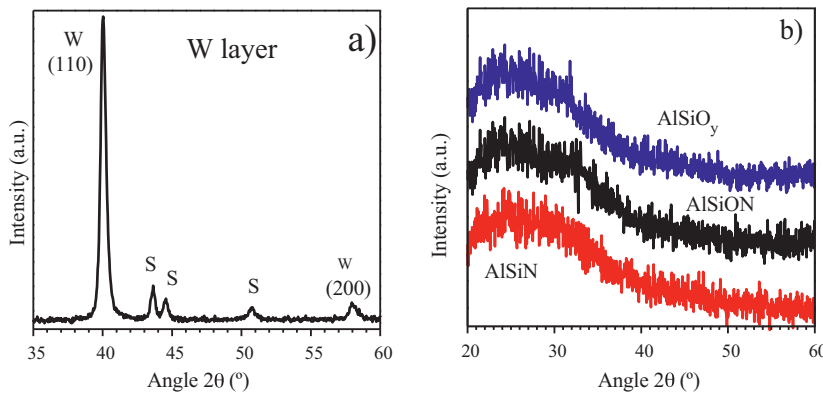


**Fig. 5.** XRD patterns of single layers performed with an incidence angle of 3° of: (a) W deposited on stainless steel and (b) AlSiN, AlSiON and AlSiO<sub>y</sub> layers, deposited on glass. S indicates the peaks associated with stainless steel substrate.

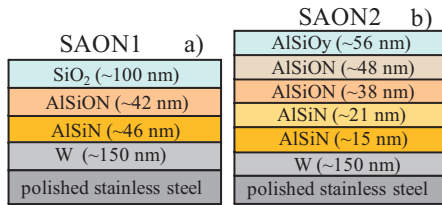


**Fig. 6.** Sketches of multilayer coatings based on AlSiN/AlSiON layers from series 1 and 2, using targets described in Table 1.

depositions were started with similar base pressures in order to reproduce the partial pressures indicated in Table 2. SAON1 and SAON4 were prepared with an Al/9Si target, the first in static mode and the second in rotation mode. SAON2 and SAON3 were prepared in static mode, with Al/15Si and Si70/Al30 targets, respectively. The spectral reflectance of these 4 coatings is shown in Fig. 7. The solar absorptance is about 94%, while the thermal emittance (at 400 °C) varies between 7 and 10%, depending on the location of the step on the wavelength scale.

### 3.5. SEM analysis of multilayered coatings

The different coatings described in Table 5, deposited on polished stainless steel substrates, were analyzed by SEM. A small piece was bent about 270° and the folded region was analyzed. In Fig. 8 are shown the micrographs obtained for SAON1 (a), SAON2 (b) and SAON4 (c) with the indication of the constituent layers of the optical stack and the respective thicknesses. In all cases, the first layer (W) shows a morphology consistent with a columnar growth. As shown by the XRD data in Section 3.3, this layer is polycrystalline. The remaining layers reveal a featureless morphology, which agrees with the amorphous structure obtained from the XRD analyses. The top layer in Fig. 8a is the antireflection layer, SiO<sub>2</sub>. The contrast difference between nitride and oxynitride layers in the SEM micrographs is very small, which does not allow a clear

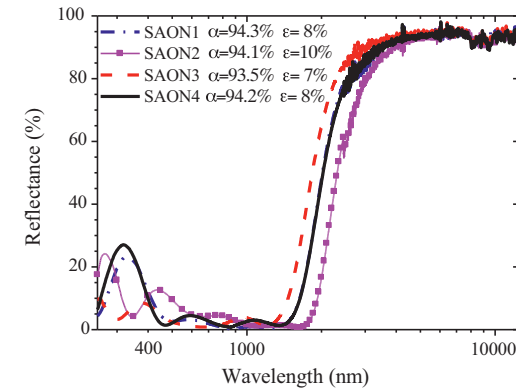


**Fig. 7.** Reflectance of different absorber coatings described in Table 5. The absorptance and thermal emittance (at 400 °C) are also indicated in the legend.

distinction between them. The thicknesses indicated in the pictures are lower than expected, 96 nm instead 100 nm for SiO<sub>2</sub> layer and 84 nm instead of 88 nm for nitride + oxynitride layers (Table 5).

For the other samples (SAON2 and SAON4), Fig. 8b and c, the antireflection layer is the AlSiO<sub>y</sub>, which was deposited with same target used for AlSiN and AlSiON layers and without breaking the vacuum. In both cases the contrast is low and it is not possible to distinguish the different layers, nitride, oxynitride and oxide. The total thicknesses of all layers, excluding W, measured by SEM are similar to those expected, which were calculated from deposition rates (Table 5).

### 3.6. Thermal stability – annealing in air and in vacuum

In Fig. 9 is represented the reflectance of different coatings (SAON1 to SAON4) in their as-deposited state and after annealing in air at 400 °C. In the legends it is indicated the solar absorptance and thermal emittance (calculated at 400 °C) for different situations. In the cases of samples prepared in static mode (SAON1 to SAON3),

**Table 5**

Partial pressures used for different layers and respective thicknesses (d) of the multilayer stacks.

SAON1		SAON2		SAON3		SAON4	
Layer	d (nm)						
W	150	W	150	W	150	W	150
N <sub>2</sub> 0.054 Pa	46	N <sub>2</sub> 0.014 Pa	15	N <sub>2</sub> 0.010 Pa	21	N <sub>2</sub> 0.047 Pa	50
N <sub>2</sub> /O <sub>2</sub> 0.077 Pa	42	N <sub>2</sub> 0.024 Pa	21	N <sub>2</sub> /O <sub>2</sub> 0.049 Pa	31	N <sub>2</sub> /O <sub>2</sub> 0.061 Pa	60
SiO <sub>2</sub>	100	N <sub>2</sub> /O <sub>2</sub> 0.045 Pa	38	N <sub>2</sub> /O <sub>2</sub> 0.077 Pa	13	O <sub>2</sub> 0.072 Pa	91
		N <sub>2</sub> /O <sub>2</sub> 0.095 Pa	48	O <sub>2</sub> 0.072 Pa	25		
		O <sub>2</sub> 0.072 Pa	56	O <sub>2</sub> 0.081 Pa	72		

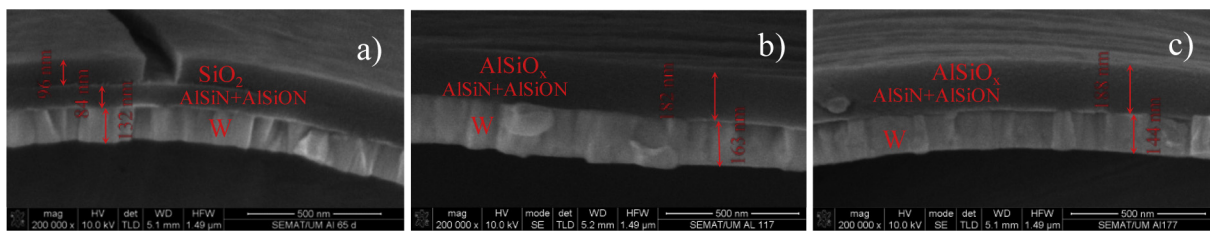


**Fig. 8.** Fractured cross section SEM images of (a) SAON1; (b) SAON2 and (c) SAON4 samples (see Table 5) deposited on stainless steel substrates. The bottom layer corresponds to W layer, and the top layer to the antireflection layer. The intermediate layer corresponds to the double layer structure (HA and LA layers), not resolved in micrographs.

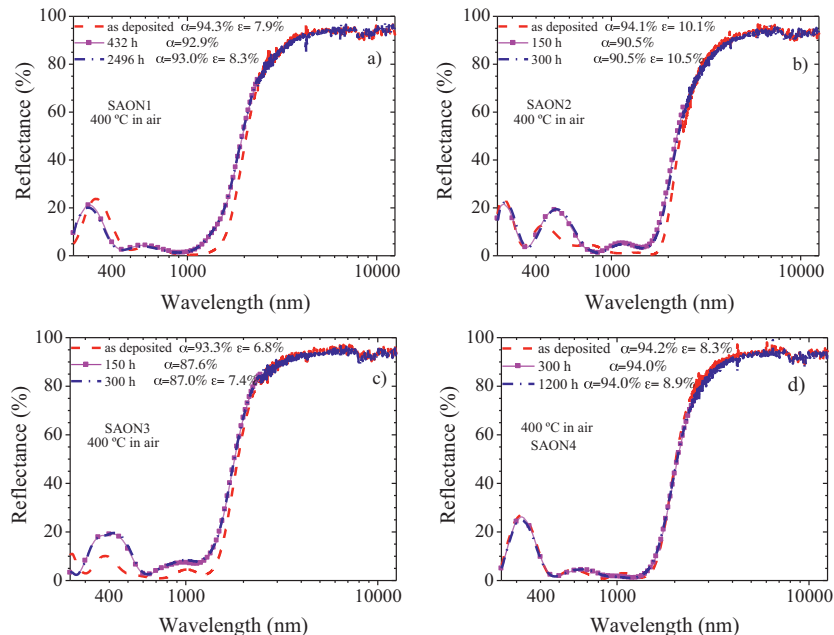


**Fig. 9.** Reflectance of as deposited coatings and after the annealing at 400 °C in air for the period indicated in the legend: (a) SAON1; (b) SAON2; (c) SAON3 (d) SAON4. The solar absorptance and the thermal emittance (calculated at 400 °C) after each annealing step are also indicated in the legend.

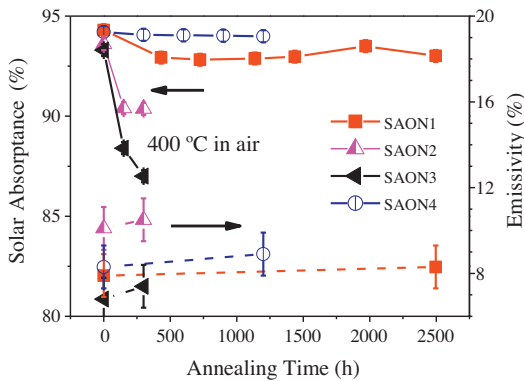


**Fig. 10.** Absorptance and thermal emittance (calculated at 400 °C) variation as a function of the annealing time for samples SAON1 to SAON4. The lines are solely introduced to guide the eyes.

the reflectance profile changed after the first annealing step. These changes induced a decrease in solar absorptance, being smaller for sample SAON1. However, the best performance was obtained for sample SAON4 prepared in rotation mode and with the same target used for SAON1.

For comparison, in Fig. 10 are shown the absorptance and thermal emittance as a function of the annealing time for all coatings. There it can be seen for sample SAON1 a decrease in solar absorptance after 432 h (~1.4%), but without significant changes after the

additional steps. However, SAON2 and SAON3 show a higher variation of solar absorptance after the first annealing step, of 3.6% and 5.7%, respectively. The solar absorptance of SAON4 did not show appreciable changes. The thermal emittance was measured in as-deposited samples and after all annealing steps. In all cases, a small increase in this value was measured (between 0.4% and 0.6%), but in the case of sample SAON1 this was registered after 2496 h, while for sample SAON4 was measured after 1200 h and for SAON2 and SAON3 after 300 h.

Similar results for thermal annealing at 580 °C, in vacuum, are shown in Fig. 11, where it is presented the solar absorptance and thermal emittance as a function of the annealing time. Again, SAON1 and SAON4 revealed better performance, but now SAON2 showed the worse performance.

These samples subjected to thermal tests were analyzed by XRD before and after the thermal annealing. The results for SAON1 sample are shown in Fig. 12. For comparison, it is also included a XRD pattern measured with a polished stainless steel substrate. As mentioned in Section 3.3, the W layer is polycrystalline while the other layers are XRD amorphous. No significant changes are seen after the annealing steps.

These samples were also studied using Raman spectroscopy. Fig. 13 shows the Raman spectra of the SAON1 and SAON3 tandem absorbers in the as-deposited form and after annealing treatments at 400 °C and 580 °C. The Raman spectra confirm the amorphous structure of the layers, presenting only three bands superposed on a broad band. The main difference between the

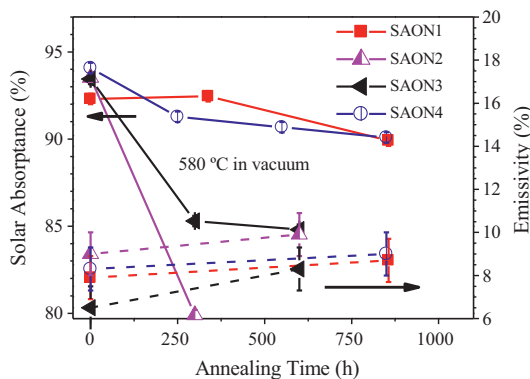


**Fig. 11.** Absorptance and thermal emittance (at 400 °C) variation as a function of the annealing time for samples SAON1 to SAON4.

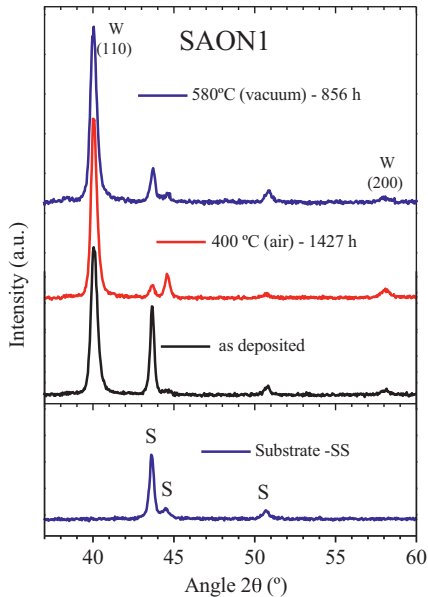


**Fig. 12.** X-ray diffraction patterns for the stainless steel substrate and sample SAON1 measured in its as-deposited state and after thermal treatments, as indicated in the figure. The measurements were performed with a fixed grazing incidence of 3°.

Raman spectra of these two groups of samples is the intensity of the Raman bands, which are better resolved in the SAON3 tandem absorber. The Raman bands peak positions are at  $\approx 150\text{ cm}^{-1}$ ,  $\approx 350\text{ cm}^{-1}$  and  $\approx 760\text{ cm}^{-1}$  for the sample SAON1 (Fig. 13a) and at  $\approx 150\text{ cm}^{-1}$  and  $\approx 450\text{ cm}^{-1}$  for the sample SAON3 (Fig. 13b). The band around  $450\text{--}460\text{ cm}^{-1}$  can be associated with silicon

rich oxynitride [38], and this is the reason why it is more pronounced in sample SAON3, which has a lower Al:Si ratio. The amorphous silicon band appears also in this region. Additionally, for these systems, the acoustic phonons (LA and TA) bands will appear in the  $150\text{--}300\text{ cm}^{-1}$  region, while the optic phonons (TO and LO) modes in the  $450\text{--}650\text{ cm}^{-1}$  region. In sample SAON3 a small shift (from  $\approx 450\text{ cm}^{-1}$  to  $\approx 460\text{ cm}^{-1}$ ) happened with the thermal annealing. This is less evident in sample SAON1, which revealed better performance. Albeit these differences between samples, for each group of samples no significant change in the nature of Raman spectra was observed, which is consistent with the high thermal microstructural stability of the produced tandem absorbers.

#### 4. Discussion

The SAON1 and SAON4 coatings were prepared with a Al/9Si target, where the Al:Si ratio in the AlSiN and AlSiON layers is  $\sim 2.3:1$ , by averaging the data obtained with XPS and EDS (Table 4). Samples SAON2 and SAON3 were prepared with lower Al:Si ratio.

Samples SAON1 and SAON4 showed the best performance. Sample SAON1 revealed a variation in solar absorptance after the first annealing step in air (432 h), as shown in Fig. 9a. This variation is associated with the oxidation of the SiOx antireflection layer, which was not completely oxidized after its deposition. Additional annealing steps (until 2496 h) did not reveal appreciable changes. The same did not occur with sample SAON4 (Fig. 9d), which has an AlSiO<sub>y</sub> antireflection layer prepared with the same target used for the underlying layers and the full stack was deposited without breaking vacuum.

The main reason for this behaviour is the chemical and thermal properties of the different layers. Silicon nitride, oxynitride and oxide are known to have good properties as diffusion barriers [40] and have also good thermal stability. AlON is also known to have good properties as gas barrier films, while SiAlON is known to have high oxidation resistance and good thermal properties. For example, amorphous SiAlON films remained amorphous after annealing in vacuum or air up to 1500 °C [18]. The film stoichiometry remained unchanged in vacuum at high temperature, although while annealing in air at 1000 °C lost some nitrogen [18]. The oxygen diffusion rate through SiAlON in N-rich samples is much faster than in O-rich case [18], which means that the oxynitride layer has much better diffusion barrier properties for oxygen than the nitride layer. Furthermore, the functionalization of an oxynitride layer with an oxide results in a good oxygen diffusion barrier that protects the non-stoichiometric nitride layer.

Other contribution comes from the structure of all films is predominantly amorphous (except for the W layer), as characterized by X-ray diffraction, both in as deposited samples and after the thermal annealing. This is a consequence of the local chemical bonding

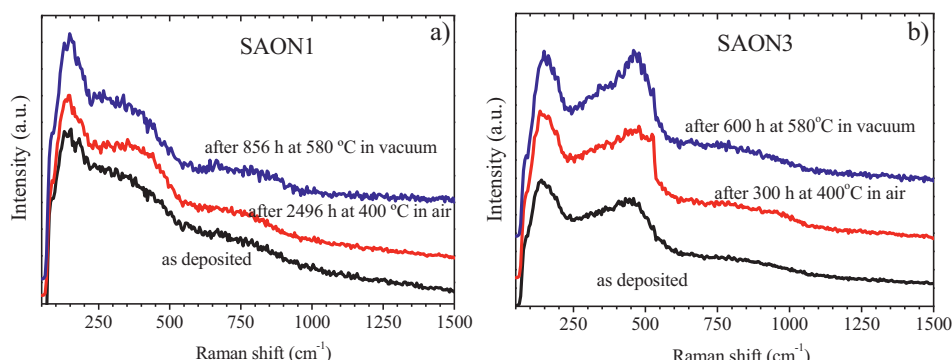


**Fig. 13.** Representative Raman spectra of SAON1 (a) and SAON3 (b) samples measured in its as-deposited state and after thermal treatments, as indicated in the figure.

effects in these materials [18], which is also important for avoiding the diffusivity paths usually present when intergranular phases are present. This improves the performance of oxide and oxynitride layers, as oxygen diffusion barrier layers.

The decrease of Al:Si contributed to a degradation of the performance. As shown, with the decrease of Al:Si ratio a non-stoichiometry was introduced to obtain the adequate spectral optical constants. For example, for samples with lower Al:Si ratio, the AlSiN layer is not sufficiently absorptive and a more graded solution employing two thin nitride layers and two thin oxynitride layers needed to be developed in order to obtain  $\alpha_s > 94\%$ . This also forced the utilization of more metallic LA layers to obtain a high solar absorptance, which also lead to a lower thermal stability of the coating. In the nonstoichiometric AlSiN films, the nitrogen amount it is not sufficient to fill all the positions in the non-metallic sublattice. Thus, Al and Si atoms occupy sites on the non-metallic sublattice, and the presence of Al–Al, Al–Si and Si–Si bonds leads to a lower chemical and thermal stability [35,39]. This non stoichiometry is the main reason for the weaker thermal stability of samples SAON2 and SAON3. For example, the shoulder that appears in the reflectance spectra around 400–500 nm after annealing in air (Fig. 9b and c) is mainly due to a small oxidation of the oxynitride layer. The reflectance in the region 700–1100 nm also increases (more evident in SAON3), which can be due to a small oxidation of the nitride layer.

All samples showed a similar increase of the thermal emittance of about 0.5% at 400 °C in air. However, at 580 °C in vacuum, the thermal emittance of samples SAON1 and SAON4 (after 900 h) increased by 0.8% and 0.7%, respectively, while for sample SAON3 it increased 2.2%. This can correspond to a small deterioration of W layer as a consequence of the lower chemical and thermal stability of the AlSiN layer produced with low N<sub>2</sub> partial pressure. This deterioration can also be associated with outwards diffusion of substrate atoms, which is related with the appearance of surface defects in samples annealed in vacuum at 580 °C. A diffusion barrier layer deposited prior the W layer would the adequate to improve the performance at these temperatures.

## 5. Summary

A tandem structure based on AlSiN and AlSiON layers for selective absorption of the solar radiation was fabricated by magnetron sputtering. The multilayer was built with a pure metallic tungsten layer, as a back reflector, followed by two absorption layers (AlSiN and AlSiON layers) and an antireflection layer (AlSiO layer). The optical stack was first simulated with the SCOUT software using suitable dielectric function models obtained from different single layers. The Al:Si ratio was changed in order to find the adequate composition for the indicated purpose. The best performance was obtained with an Al:Si ratio in the AlSiN and AlSiON layers of about 2.3:1. The samples were subjected to a thermal annealing at 400 °C and 580 °C, in air and vacuum, respectively. The tandem structure with that adequate Al:Si ratio revealed good solar selective properties, as well as good thermal stability.

With the increase of Si content it was necessary to decrease the reactive gases content in order to get sufficient absorption of the solar radiation and Al–Al, Al–Si and Si–Si chemical bonds were found in the AlSiN layers, as shown by XPS analysis. These bonds lead to lower chemical and thermal stability of the overall structure. The AlSiN and AlSiON films with different Al:Si ratio revealed to be completely miscible and do not result in phase separation at the tested annealing process. X-ray photoelectron analysis indicates preferential formation of local Al–O and Si–N bonds, which has been shown to stabilize the amorphous structure.

## Acknowledgements

The authors acknowledge the funding from the Finnish Funding Agency for Technology and Innovation, Tekes, and from FEDER funds through the “Programa Operacional Factores de Competitividade – COMPETE” and from national funds by FCT – “Fundação para a Ciência e a Tecnologia”, under project no. PEst-C/FIS/UI0607/2011.

## References

- [1] H.G. Craighead, R.A. Buhrman, Optical-properties of selectively absorbing Ni-Al<sub>2</sub>O<sub>3</sub> composite films, *Appl. Phys. Lett.* 31 (1977) 423–425.
- [2] B.O. Seraphin, Chemical vapor deposition of thin semiconductor films for solar energy conversion, *Thin Solid Films* 39 (1976) 87–94.
- [3] W.F. Bogaerts, C.M. Lampert, Materials for photothermal solar energy conversion, *J. Mater. Sci.* 18 (1983) 2847–2875.
- [4] C.E. Kennedy, Review of Mid- to High-Temperature Solar Selective Absorber Materials, NREL/TP-520-31267, National Renewable Energy Laboratory, Golden, CO, 2002.
- [5] M. Lanxner, Z. Elgat, Solar selective absorber coatings for high service temperatures, produced by plasma sputtering, *Proc. Soc. Photo-Opt. Instrum. Eng.* 1272 (1990) 240–249.
- [6] Q.C. Zhang, D.R. Mills, Very low-emittance solar selective surfaces using new film structures, *J. Appl. Phys.* 72 (1992) 3013–3021.
- [7] Y. Yin, R.E. Collins, Optimization and analysis of solar selective surfaces with continuous and multilayer profiles, *J. Appl. Phys.* 77 (1995) 6485–6491.
- [8] M. Farooq, M.G. Hutchins, A novel design in composites of various materials for solar selective coatings, *Solar Energy Mater. Solar Cells* 71 (2002) 523–535.
- [9] H.G. Craighead, R. Bartynski, R.A. Buhrman, L. Wojcik, A.J. Sievers, Metal–insulator composite selective absorbers, *Solar Energy Mater.* 1 (1979) 105–124.
- [10] C.G. Granqvist, O. Hunderi, Optical properties of Ag–SiO<sub>2</sub> Cermet films: a comparison of effective-medium theories, *Phys. Rev. B* 18 (1978) 2897.
- [11] G.A. Niklasson, Optical properties of inhomogeneous two-component materials, in: C.G. Granqvist (Ed.), *Materials Science for Solar Energy Conversion Systems*, Pergamon, Oxford, 1991, pp. 7–43.
- [12] Qi-Chu Zhang, Y.G. Shen, High performance W–AlN cermet solar coatings designed by modelling calculations and deposited by DC magnetron sputtering, *Solar Energy Mater. Solar Cells* 81 (2004) 25–37.
- [13] A. Antoniaia, A. Castaldo, M.L. Addonizio, S. Esposito, Stability of W-Al<sub>2</sub>O<sub>3</sub> cermet based solar coating for receiver tube operating at high temperature, *Solar Energy Mater. Solar Cells* 94 (2010) 1604–1611.
- [14] H.C. Barshilia, N. Selvakumar, K.S. Rajam, Thermal stability of TiAlN/TiAlON/Si<sub>3</sub>N<sub>4</sub> tandem absorbers prepared by reactive direct current magnetron sputtering, *J. Vac. Sci. Technol. A25* (2007) 383–390.
- [15] Miao Du, Lei Hao, Jing Mi, Fang Lv, X. Liu, L. Jiang, S. Wang, Optimization design of Ti<sub>0.5</sub>Al<sub>0.5</sub>N/Ti<sub>0.25</sub>Al<sub>0.75</sub>N/AlN coating used for solar Selective applications, *Solar Energy Mater. Solar Cells* 95 (2011) 1193–1196.
- [16] L. Rebouta, A. Pitões, M. Andritschky, P. Capela, M.F. Cerqueira, A. Matilainen, K. Pischow, Optical characterization of TiAlN/TiAlON/SiO<sub>2</sub> absorber for solar selective applications, *Surf. Coat. Technol.* 211 (2012) 41–44.
- [17] T. Ekström, M. Nygren, SiAlON ceramics, *J. Am. Ceram. Soc.* 75 (1992) 259–276.
- [18] R.J. Lad, Multifunctional Silicon Aluminum Oxynitride (SiAlON) Ceramic Coatings for High Temperature Applications, Final performance Report, AFOSR Grant # F49620-02-1-0323, 2006.
- [19] L. Rebouta, P. Capela, M. Andritschky, A. Matilainen, P. Santilli, K. Pischow, E. Alves, Characterization of TiAlSiN/TiAlSiON/SiO<sub>2</sub> optical stack designed by modelling calculations for solar selective applications, *Solar Energy Mater.* Solar Cells 105 (2012) 202–207.
- [20] T.C. Paulick, Inversion of normal-incidence (*R*, *T*) measurements to obtain *n*+*ik* for thin films, *Appl. Opt.* 25 (1986) 562–564.
- [21] M. Fox, *Optical Properties of Solids*, Oxford University Press Inc., New York, 2001.
- [22] W. Theiss, in: M. Theiss (Ed.), *SCOUT Thin Film Analysis Software Handbook*, Hard- and Software, Aachen, Germany, 2002.
- [23] M.P. Seah, T.S. Nunney, Sputtering yields of compounds using argon ions, *J. Phys. D: Appl. Phys.* 43 (2010) 253001.
- [24] E. Hollands, D.S. Campbell, The mechanism of reactive sputtering, *J. Mater. Sci.* 3 (1968) 544–552.
- [25] C.R. Werrett, D.R. Pyke, A.K. Bhattacharya, XPS studies of oxide growth and segregation in aluminium–silicon alloys, *Surf. Interface Anal.* 25 (1997) 809–816.
- [26] H. Li, A. Belkind, F. Jansen, Z. Orban, An in situ XPS study of oxygen plasma cleaning of aluminum surfaces, *Surf. Coat. Technol.* 92 (1997) 171–177.
- [27] W. Österle, I. Dörfel, I. Urban, T. Reier, J.W. Schultze, XPS and XTEM study of AlN formation by N<sup>+</sup><sub>2</sub> implantation of aluminium, *Surf. Coat. Technol.* 102 (1998) 168–174.
- [28] I. Bertoti, Characterization of nitride coatings by XPS, *Surf. Coat. Technol.* 151–152 (2002) 194–203.

- [29] A. Pelisson-Schecker, H.J. Hug, J. Patscheider, Charge referencing issues in XPS of insulators as evidenced in the case of Al–Si–N thin films, *Surf. Interface Anal.* 44 (2012) 29–36.
- [30] J. Dupuis, E. Fourmond, D. Ballutaud, N. Bererd, M. Lemiti, Optical and structural properties of silicon oxynitride deposited by plasma enhanced chemical vapor deposition, *Thin Solid Films* 519 (2012) 1325–1333.
- [31] P. Cova, S. Poulin, O. Grenier, R.A. Masut, A method for the analysis of multiphase bonding structures in amorphous  $\text{SiO}_x\text{N}_y$  films, *J. Appl. Phys.* 97 (2005) 073518.
- [32] S. Ladas, L. Sygellou, S. Kennou, M. Wolf, G. Roeder, A. Nutsch, M. Rambach, W. Lerch, An X-ray photoelectron spectroscopy study of ultra-thin oxynitride films, *Thin Solid Films* 520 (2011) 871–875.
- [33] M.C. Poon, C.W. Kik, W. Wong, P.J. Chard, Bonding structures of silicon oxynitride prepared by oxidation of Si-rich silicon nitride, *Thin Solid Films* 462–463 (2004) 42–45.
- [34] S. Shinagawa, H. Nohira, T. Ikuta, M. Hori, M. Kase, T. Hattori, Angle-resolved XPS study on chemical bonds in ultrathin silicon oxynitride films, *Microelectron. Eng.* 80 (2005) 98–101.
- [35] F. Vacandio, Y. Massiani, P. Gravier, A. Garnier, A study of the physical properties and electrochemical behaviour of aluminium nitride films, *Surf. Coat. Technol.* 92 (1997) 221–229.
- [36] J. Ushio, T. Maruizumi, K. Kushida-Abdelghafar, Interface structures generated by negative-bias temperature instability in  $\text{Si}/\text{SiO}_2$  and  $\text{Si}/\text{SiO}_x\text{N}_y$  interfaces, *Appl. Phys. Lett.* 81 (2002) 1818–1820.
- [37] J.P. Chang, M.L. Green, V.M. Donnelly, R.L. Opila, J. Eng Jr., J. Sapjeta, P.J. Silverman, B. Weir, H.C. Lu, T. Gustafsson, E. Garfunkel, Profiling nitrogen in ultrathin silicon oxynitrides with angle-resolved X-ray photoelectron spectroscopy, *J. Appl. Phys.* 87 (2000) 4449–4455.
- [38] R.A.R. Oliveira, M. Ribeiro, I. Pereyra, M.I. Alayo, Silicon clusters in PECVD silicon-rich  $\text{SiO}_x\text{N}_y$ , *Mater. Charact.* 50 (2003) 161–166.
- [39] H.P. Lobl, M. Huppertz, Thermal stability of nonstoichiometric silicon nitride films made by reactive dc magnetron sputter deposition, *Thin Solid Films* 317 (1998) 153–156.
- [40] M. Vogt, M. Kachel, M. Plötner, K. Drescher, Dielectric barriers for Cu metallization systems, *Microelectron. Eng.* 37–38 (1997) 181–187.